Passive scalar mixing near turbulent/non-turbulent interface in compressible turbulent boundary layers

Xinxian Zhang[1], **Tomoaki Watanabe**[1]‡**, and Koji Nagata**[1]

[1]Department of Aerospace Engineering, Nagoya University, Nagoya, Japan

E-mail: `watanabe.tomoaki@c.nagoya-u.jp`

August 2018

Abstract. Direct numerical simulations for compressible temporally evolving turbulent boundary layers at Mach number of $M = 0.8$ and 1.6 are preformed up to the Reynolds number based on the momentum thickness $Re_\theta \approx 2200$ to investigate a passive scalar field near the turbulent/non-turbulent interface (TNTI) layer that is formed at the edge of the turbulent boundary layers. The passive scalar is diffused from the wall in the turbulent boundary layers developing on the moving wall at constant speed. The outer edge of the TNTI layer detected by an isosurface of vorticity magnitude and passive scalar are compared by visualization, and it is shown that the passive scalar can be used for detecting the TNTI layer in compressible boundary layers. Conditional statistics are calculated as a function of the distance from the outer edge of the TNTI layer. The mean thicknesses of TNTI layer, viscous superlayer (VSL), and turbulent sublayer (TSL), is about $15\eta_I$, $4\eta_I$, and $11\eta_I$, respectively (η_I: Kolmogorov length scale in the turbulent core region near the TNTI layer). The conditional mean profiles of scalar dissipation rate have a large peak near the boundary between the VSL

---

‡ Corresponding author: watanabe.tomoaki@c.nagoya-u.jp

and TSL, where the fluid with a low scalar value locally entrained from non-turbulent region encounters the turbulent fluid with a higher scalar value. The scalar dissipation rate near the TNTI depends on the TNTI orientation: it is larger near the TNTI facing the downstream direction with respective to the mean flow in the boundary layer (leading edge). This is partially explained by the dependence of the production rate of passive scalar gradient. The conditional mean production rate of the scalar dissipation rate near the leading edge is as large as in the turbulent core region while it is close to the non-turbulent value when the TNTI faces the upstream region (trailing edge).

PACS numbers: 47.27.tb, 47.51.+a, 47.27.ep

Submitted to: *Phys. Scr.*

1. Introduction

Compressible turbulent boundary layers (TBLs) often appear in engineering applications and science. For example, in an aircraft turbine engine, a compressible TBL developed on each blade affects an overall power produced by the turbine [1]. A compressible TBL is also significantly related to the weather prediction and substance diffusion in atmosphere [2], which are all important issues in atmospheric science [3]. High-speed boundary layer also appears in propulsion system, where mixing of fuel in the boundary layer can affect the combustion [4, 5]. Turbulence developing on a wall can significantly contribute mixing of scalar, such as mass fraction of chemical substances. This is because the nature of turbulence that creates a small-scale fluctuating scalar field, which enhances mixing at molecular level. Modeling of turbulent mixing is crucial in numerical simulations of reacting flows [6]. One of the key quantiles in modeling of turbulent reacting flows is scalar dissipation rate, which strongly depends on the characteristics of turbulence [7]. Many models developed for simulating turbulent reacting flows contain scalar dissipation rate as an unknown variable [8, 9, 10, 11, 12].

Turbulent boundary layers are known as highly intermittent flows, where both turbulent and non-turbulent (laminar) fluids coexist. The spatial distribution of turbulent fluids plays an important role in scalar mixing in TBLs. Turbulent and non-turbulent fluids are separated by a thin layer, which is called turbulent/non-turbulent interface (TNTI) layer [13, 14]. The TNTI layer is also found in other canonical flows, e.g., jet, mixing layer, and wake [15, 16, 14]. Recent studies have shown that the TNTI layer consists of two layers [15]: one is called viscous superlayer (VSL), in which the viscous term dominates the growth of enstrophy; another one is the buffer layer called as turbulent sublayer (TSL) between the VSL and turbulent core region. Transport processes of various quantities, e.g., mass, heat, kinetic energy, and momentum, across the TNTI layer is important because of very different characteristics between turbulent and non-turbulent fluids. The TNTI layer is related to the mass entrainment rate in various turbulent flows [15], and therefore, statistical properties of turbulence near the TNTI layer are expected to be important for developing models for entrainment and numerical simulations. However, the TNTI in TBLs has not been well studied compared to free shear flows, even though some characteristics of the TNTI in TBLs are found to be similar to other flows.

Passive scalar mixing in a fluid is enhanced by turbulence. This can be seen as high dissipation rate of the scalar fluctuation. Because the TNTI often appears near the interface that separates two streams with different chemical substances, the mixing process near the TNTI is also important in chemically reacting flows [17, 18, 19], where the chemical reaction rate is strongly affected by turbulence. Therefore, it is important to investigate the characteristics of passive scalar mixing near the TNTI.

In present study, we perform direct numerical simulations (DNSs) for temporally evolving compressible turbulent boundary layers at subsonic and supersonic Mach number with a passive scalar transfer. The statistical properties of passive scalar are studied in relation to the TNTI, where the TNTI orientation with respective to the mean flow in the boundary layer is shown to be important in enhancement of mixing by turbulence near the TNTI. The details of DNS are described in Sec. 2. Sec. 3

presents fundamental statistics of the TBL as well as statistics related to the TNTI layer, whose outer edge called irrotational boundary, is detected by an isosurface of vorticity magnitude. Finally, Sec. 4 summarizes the conclusion.

2. Direct numerical simulation

2.1. Temporally evolving compressible boundary layers

We use the DNS database used in our previous study [20], where DNS was performed for temporally evolving compressible TBLs. Here, we present the details of the simulations. Temporally evolving TBLs have been shown to be a good model of spatially evolving TBLs [21, 22]. For example, a vertical profile of most statistics in the fully developed region is quite similar between spatial and temporal TBLs [21, 22]. It was also shown that the averaged momentum equation is also dominated by the same term in both boundary layers, and therefore, the growth of the TBL thickness defined by the mean streamwise velocity is caused by the same mechanism [22].

The temporally evolving TBL develops with time in the computational domain that is periodic in the streamwise and spanwise directions. The governing equations are compressible Navier–Stokes equations and scalar transport equation:

$$\frac{\partial \rho}{\partial t} + \frac{\partial \rho u_j}{\partial x_j} = 0, \tag{1}$$

$$\frac{\partial \rho u_i}{\partial t} + \frac{\partial \rho u_i u_j}{\partial x_j} = -\frac{\partial P}{\partial x_i} + \frac{\partial \tau_{ij}}{\partial x_j}, \tag{2}$$

$$\frac{\partial \rho T}{\partial t} + \frac{\partial \rho T u_j}{\partial x_j} = (1-\gamma) P \frac{\partial u_j}{\partial x_j} + \gamma \frac{\partial}{\partial x_j}\left(k \frac{\partial T}{\partial x_j}\right) + (\gamma - 1)\tau_{ij}\frac{\partial u_i}{\partial x_j}, \tag{3}$$

$$\frac{\partial \rho \phi}{\partial t} + \frac{\partial \rho u_j \phi}{\partial x_j} = \frac{\partial}{\partial x_j}\left(\rho D_m \frac{\partial \phi}{\partial x_j}\right), \tag{4}$$

with the equation of state for the perfect gas $P = \rho R T$. τ_{ij} is the viscous stress tensor represented by

$$\tau_{ij} = \mu\left(\frac{\partial u_i}{\partial x_j} + \frac{\partial u_j}{\partial x_i} - \frac{2}{3}\delta_{ij}\frac{\partial u_k}{\partial x_k}\right). \tag{5}$$

Here ρ is the density, u_i is the velocity, P is the pressure, T is the temperature, k is the thermal conductivity, D_m is the molecular diffusivity for the passive scalar ϕ, $\gamma = 1.4$ is the ratio of specific heats, and $R = 287$ [J/(kg · K)] is the gas constant.

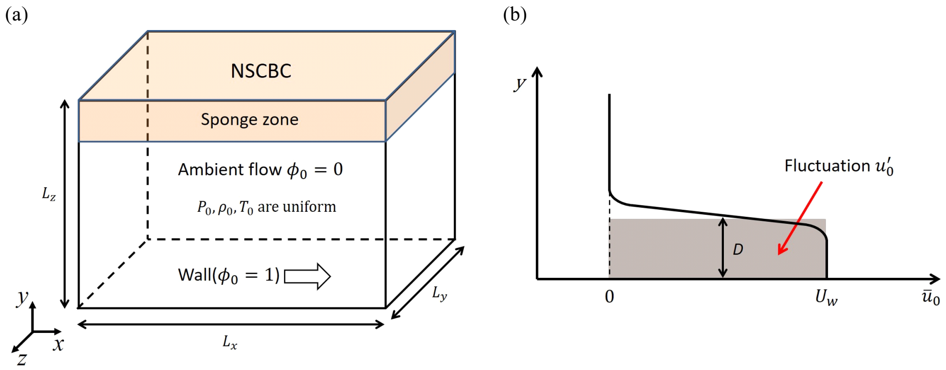

Figure 1. (a) Computational domain. (b) Initial streamwise velocity profile.

We assume that the Prandtl number $Pr = \mu C_p/k = 0.71$ and the Schmidt number $Sc = \mu/\rho D_m = 1$, where μ is the viscosity computed as a function of temperature T by the Sutherland's law with $\mu_s = 1.742 \times 10^{-5}$ (Pa·s), $T_s = 273$ (K), and $S = 110.4$ (K):

$$\mu = \mu_s \left(\frac{T}{T_s}\right)^{3/2} \frac{T_s + S}{T + S}. \tag{6}$$

The computational domain is a rectangular box with the size of $(L_x \times L_y \times L_z)$ as shown in Fig. 1(a). The bottom of the computational domain is the wall over which the TBL develops. The origin of the coordinate system is located at the center of the wall. The streamwise, wall-normal, and spanwise directions are represented by x, y, and z, respectively. We consider the TBL developing over the wall moving in the x direction at a constant speed U_w. Hereafter, subscript w represents a quantity on the wall. The initial velocity field approximates the velocity induced by a trip wire installed on the wall with a diameter D [23]. The trip wire is often used in experiments to promote the transition from laminar to turbulent boundary layer [24]. In the temporally evolving boundary layers, average can be calculated on a wall-parallel plane as a function of y and t. A flow variable f can be expressed by average $\overline{f}(y,t)$ and fluctuation $f'(x,y,z,t)$ as $f(x,y,z,t) = \overline{f}(y,t) + f'(x,y,z,t)$. Hereafter, the subscript 0 refers to values at $t = 0$. The initial velocity $\mathbf{u}_0(x,y,z)$ consists of the mean velocity $\overline{\mathbf{u}}_0 = (\overline{u}_0(y), 0, 0)$ and fluctuating components $\mathbf{u}_0'(x,y,z)$. $\mathbf{u}_0'(x,y,z)$

has non zero values for $y < D$ to trigger turbulent transition, and it is generated by the method based on a diffusion equation [25], by which random noise is converted into fluctuations with a prescribed length scale. The initial mean streamwise velocity profile $\overline{u}_0(y)$ is given by a hyperbolic tangent profile [23] so that $\overline{u}_0$ is equal to the wall velocity U_w at $y = 0$ and decreases toward 0 in the wall normal direction:

$$\overline{u}_0(y) = \frac{U_w}{2} + \frac{U_w}{2} \tanh\left[\frac{D}{2\theta_{sl}}\left(1 - \frac{y}{D}\right)\right], \tag{7}$$

where, $\theta_{sl} = 0.1D$ is the initial shear layer thickness. The mean velocity profile is shown in Fig. 1(b). Temperature, pressure, and density are uniform at the initial state, where $T_0 = 300$ (K), $P_0 = 101.3$ (kPa), and $\rho_0 = P_0/RT_0$. The initial profile of ϕ is uniform in the wall parallel direction, and is given by the hyperbolic tangent profile similar to Eq. (7), where ϕ_0 is equal to 1 on the wall ($y = 0$) and ϕ_0 decreases toward 0 as y increases. The Reynolds number based on the trip wire diameter D is $Re_D \equiv \rho_0 U_w D/\mu_0 = 2000$, which is much larger than the critical value for turbulent transition ($Re_D = 500$) in temporally evolving incompressible TBLs [23]. The Mach number is defined as $M = U_w/c_0$, where c_0 is the speed of sound at the initial state. DNSs are performed for $M = 0.8$ and 1.6, which are subsonic and supersonic boundary layers, respectively. The values of U_w and D are determined from (Re_D, M). The DNSs of $M = 0.8$ and 1.6 consider the flow with $U_w = 277.75$ (m/s) and $D = 1.136 \times 10^{-4}$ (m) and with $U_w = 555.50$ (m/s) and $D = 5.678 \times 10^{-5}$ (m), respectively.

2.2. Numerical methods used in DNS code

The sets of explicit numerical schemes presented in Wang et al [26] are used in present DNS code. For time integration, the Euler terms are treated with the explicit 5-stage 4th-order Runge-Kutta method [27] and the other terms are treated with the explicit 1st-order Euler scheme. For the spatial discretization, the explicit 8th-order center-difference scheme is used for the interior nodes, while the nodes near the computational boundaries are treated with internal-biased lower-order finite difference schemes for stability unless the periodic boundary conditions are applied. Finally, for removing the spurious fluctuations induced by the central difference scheme, a 10th-order explicit low-pass filter [28] is applied to ρ, ρu, ρv, ρw, and ρT in the whole computational domain at each time step.

In the DNS of temporally evolving TBLs, the periodic boundary conditions are applied in the streamwise (x) and spanwise (z) directions. The wall is treated with the non-slip adiabatic condition, while the non-reflective outflow boundary conditions of 3D Navier–Stokes characteristics boundary conditions [29] are applied at the top of the computational domain ($y = L_y$) with a sponge layer [30] in the region of $L_y - 10D < y < L_y$ to prevent the spurious wave reflections on the boundary. The explicit 2nd-order low pass filter [31] is applied in the sponge layers in addition to the 10th-order explicit low-pass filter.

The time step interval is determined by the Courant Friedrichs Lewy (CFL) condition with the instantaneous velocity and sound speed as below and the CFL = 0.8 is used in this study.

$$\Delta t = \mathrm{CFL}\times\min\left\{1 \Bigg/ \left[\sqrt{\gamma R T_0\left(\frac{1}{\Delta x^2}+\frac{1}{\Delta y^2}+\frac{1}{\Delta z^2}\right)}+\frac{u}{\Delta x}+\frac{v}{\Delta y}+\frac{w}{\Delta z}\right]\right\}. \quad (8)$$

These numerical schemes were used in the DNS of subsonic round jet [31], diffusion jet flame [26], and supersonic planar jets [12, 32], which succeeded in reproducing the statistics in consistent with experiments.

2.3. Computational parameters in DNS

The governing equations are integrated in time until the Reynolds number based on the momentum thickness, $Re_\theta = \rho_\infty U_w \theta/\mu_\infty$, reaches about 2200, which is high enough to have the fully-developed TBLs. In the present DNS, the flows turn into fully-developed turbulent boundary layers at $t/(D/U_w) \approx 230$ for $M = 0.8$ and $t/(D/U_w) \approx 250$ for $M = 1.6$, in the sense that the friction coefficient plotted against the momentum thickness Reynolds number begins to follow the friction law for turbulent boundary layers [20]. The momentum thickness Reynolds number has $Re_\theta \approx 1200$ at these time instances. Here the subscript ∞ refers to the properties in the freestream and the momentum thickness is defined as $\theta = \int_0^\infty (\overline{\rho u}/\rho_\infty U_w)\left[1 - (\overline{u}/U_w)\right] dy$.

The computational domain size ($L_x \times L_y \times L_z$) should be large enough to contain the large-scale flow structures for preventing periodic boundaries from having non-physical effects on the flow development. L_x, L_y, and L_z in the present DNS are determined based on the boundary layer thickness δ at $Re_\theta \approx 2200$, where δ is defined as the vertical location y at which the streamwise mean velocity $\overline{u}$ reduces to 1% of the wall velocity U_w [33]. Following to Kozul et al [23], we determine (L_x, L_y, L_z) so that $L_x \approx 6\delta$, $L_z \approx 3\delta$, and $L_y \approx 3\delta + 10D$ (here $10D$ is the thickness of the sponge layer).

The Cartesian mesh is used in this study. The grid spacing is uniform in the x and z directions, while the wall-normal grid spacing obeys a half-tanh mapping, which gives a finer grid near the wall. For studying the TNTI, the resolution near the TNTI should be carefully examined, where the DNS must resolve the smallest scale of turbulence that appears underneath the TNTI, i.e., Kolmogorov scale $\eta = (\overline{\nu}^3/\overline{\varepsilon})^{1/4}$ in the turbulent region [$\varepsilon = \tau_{ij} S_{ij}$ is the kinetic energy dissipation rate; $S_{ij} = (\partial u_i/\partial x_j + \partial u_j/\partial x_i)/2$ is the rate of strain tensor; $\nu = \mu/\rho$ is the kinematic viscosity]. The number of the grid points (N_x, N_y, N_z) is determined by comparing the spatial resolution with the viscous length scale δ_ν on the wall and the Kolmogorov scale η_c at $y = 0.5\delta$, which is in the turbulent core region away from the wall. Here subscript c denotes a value in the turbulent core region at $y = 0.5\delta$, and the viscous length scale is defined as $\delta_\nu = \overline{\nu}_w/u_\tau$ with the friction velocity $u_\tau = \sqrt{\tau_w/\overline{\rho}_w}$ and the wall shear stress $\tau_w \equiv \overline{\mu}_w(-d\overline{u}/dy)_w$. We ensure that the mesh size satisfies $\Delta x^+ < 4.8$, $\Delta y_w^+ < 0.2$, and $\Delta z^+ < 4.8$. Here, the quantities with superscript + are normalized by the viscous scale. With these criteria, the grid spacing in the streamwise direction is smaller than the DNS of wall turbulence in existing literatures [34]. It was shown that a coarser grid in the streamwise direction, $\Delta x^+ \approx 8$, often used in DNS of wall turbulence, does not have a resolution enough to resolve the Kolmogorov scale in the intermittent region, where the TNTI exists [35].

(L_x, L_y, L_z) and (N_x, N_y, N_z) are determined based on the above discussion, and are summarized in Tab. 1, which also includes Re_θ and the friction Reynolds number

Table 1. Computational parameters and Reynolds numbers obtained in fully developed turbulent states of boundary layers for which detail analysis is performed.

M	Re_θ	Re_τ	L_x/δ, L_y/δ, L_z/δ	Δx^+, Δy_w^+, Δz^+	N_x, N_y, N_z
0.8	2206	639	6.30, 5.37, 3.15	4.6, 0.188, 4.6	972, 738, 486
1.6	2174	524	7.23, 5.92, 3.62	4.9, 0.180, 4.6	972, 772, 512

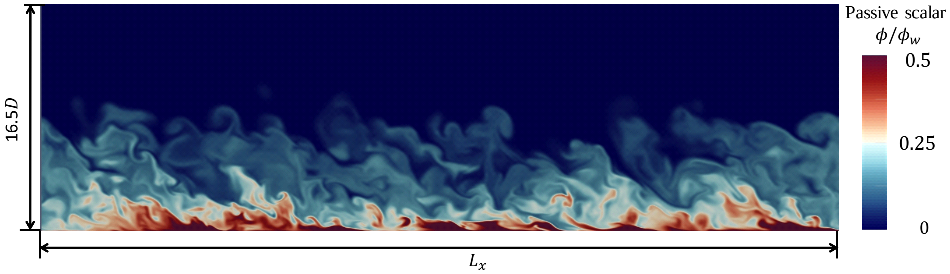

Figure 2. Visualization of instantaneous value of passive scalar ϕ on a $x-y$ plane at $z=0$ in temporally evolving compressible boundary layer at $M=0.8$ and $Re_\theta=2152$ ($Re_\tau=622$). The wall is moving in the x direction (from left to right).

$Re_\tau = \overline{\rho}_w u_\tau \delta/\overline{\mu}_w$ at the end of the simulation, at which the TBLs are analyzed in detail.

3. Results and Discussion

3.1. Comparison with spatially evolving TBLs

The passive scalar ϕ can be considered as a marker of the turbulent region ($\phi > 0$) [36], which allows us to visualize the distribution of turbulent fluids by ϕ as shown in Fig. 2 for $M = 0.8$. We can see in the intermittent region, where non-turbulent fluids with $\phi = 0$ coexist with the turbulent fluids $\phi > 0$ at the same height.

Van Driest transformed [40] mean streamwise velocity u_{VD} and passive scalar ϕ_{VD} are plotted in Fig. 3(a) for comparing the statistics at different Mach numbers. The definition of Van Driest transformed [40] mean streamwise velocity u_{VD} is given as:

$$u_{VD}(y) = \int_0^{u^+} \sqrt{\frac{\overline{\rho}(y)}{\overline{\rho}_w}} du^+, u^+(y) = [U_w - \overline{u}(y)]/u_\tau. \tag{9}$$

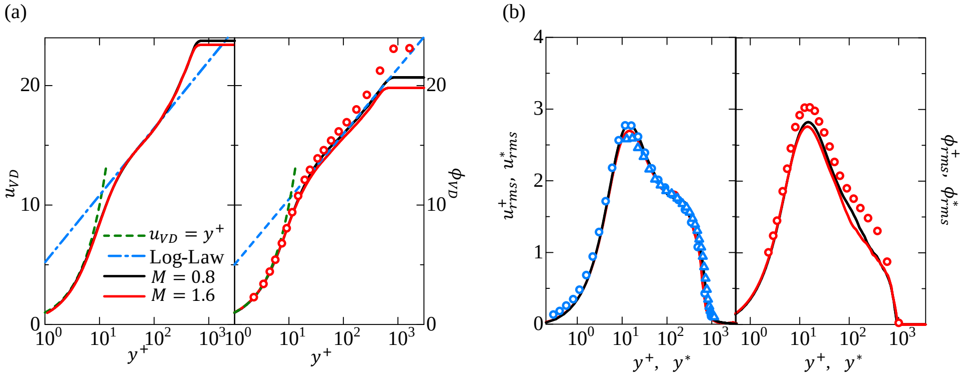

Figure 3. Vertical profiles of (a) Van Driest transformed mean streamwise velocity and passive scalar, (b) rms streamwise velocity and scalar fluctuations. The DNS (○ [37]; ○ [38]) and experiment (△ [39]) of spatially evolving incompressible turbulent boundary layers are compared with the present DNS.

Similarly, Van Driest transformed [40] mean passive scalar is

$$\phi_{VD}(y) = \int_0^{\phi^+} \sqrt{\frac{\overline{\rho}(y)}{\overline{\rho}_w}} d\phi^+, \phi^+(y) = [\phi_w - \overline{\phi}(y)]/\phi_\tau, \tag{10}$$

with $\phi_\tau \equiv \overline{D}_m(-d\overline{\phi}/dy)_w/u_\tau$. In the viscous sublayer ($y^+ < 5$), the Reynolds shear stress is negligible compared to the viscous stress and the DNS data agree well with the green dot line ($u_{VD} = y^+$); in the log-law region, the present DNS results are in a good agreement with red dash line represented as $u_{VD} = (1/k)\ln y^+ + A$ [33] with the constants $k = 0.41$ and $A = 5.1$. ϕ_{VD} is compared with DNS of spatially evolving incompressible TBL [38]. Similarly, ϕ_{VD} follows $\phi_{VD} = y^+$ in the viscous sublayer ($y^+ < 5$), while the log-law $\phi_{VD} = (1/k)\ln y^+ + A$ is also valid in the log-law region for $\overline{u}$. These features of the mean scalar profile can be also seen in the DNS of spatially evolving incompressible TBL.

The second-order statistics are compared with experimental data [39] and other DNS data [37] of spatially evolving incompressible TBLs in Fig. 3(b). As described in Morkovin's hypothesis [41], the compressibility mainly affects the density and thermodynamic properties across the boundary layer rather than time scale and length scale of turbulence for moderate Mach number $M < 5$ [3]. Therefore, compressible TBLs are often compared with incompressible TBLs at a similar Re_θ by transforming second-order velocity statistics by [42]:

$$u^*_{i,rms} = \sqrt{\frac{\widetilde{u''_i u''_i}}{u_\tau^2}\frac{\overline{\rho}(y)}{\overline{\rho}_w}}; \quad u''_i = u_i - \widetilde{u}_i; \tag{11}$$

$$y^* = y/\delta^*_\nu; \quad \delta^*_\nu(y) = \overline{\nu}(y)/(u_\tau\sqrt{\overline{\rho}_w/\overline{\rho}(y)}), \tag{12}$$

where $\widetilde{f}$ is a density-weighted average (Favre average): $\widetilde{f} = \overline{\rho f}/\overline{\rho}$. Similar transformation can be defined for ϕ by replacing u_i and u_τ by ϕ and ϕ_τ, respectively. As shown in Fig. 3 (b), we can find good agreements, for the root-mean-squared (rms) streamwise velocity fluctuation and scalar fluctuation for a comparable value of Re_θ. Note that the mean velocity, rms velocity fluctuations, and passive scalar fluctuations in the compressible boundary layers presented above are consistent with those in incompressible boundary layers only after applying the Van Driest transformation.

Further validation of the present DNS database was presented in our previous paper [20], where vertical rms velocity fluctuation, Reynolds stress, skin friction coefficient, and mass entrainment rate per a unit horizontal area were also shown to be consistent with spatially evolving TBL.

3.2. Detection of Turbulent/non-turbulent interface

As shown in previous studies of the TNTI [43], we use an isosurface of vorticity magnitude $\omega = \omega_{th}$ to detect the outer edge of the TNTI layer called the irrotational boundary. The threshold ω_{th} is determined based on the volume fraction of the turbulent region normalized by the computational domain size (V_T), in which a fluid with $\omega > \omega_{th}$ is referred to as a turbulent fluid while a non-turbulent fluid has $\omega < \omega_{th}$. This approach is proved to be able to detect the outer edge of the TNTI layer in both incompressible and compressible flows [43, 44]. V_T computed as a function of ω_{th} as shown in Fig. 4, where $\hat{\omega}_{th}$ is vorticity magnitude normalized by the mean vorticity magnitude $\overline{\omega}_c$ at $y = 0.5\delta$. In the figure, we can see that the turbulent volume V_T hardly changes with $\hat{\omega}_{th}$ in the range of $10^{-4} < \hat{\omega}_{th} < 10^{-1}$ for both Mach numbers. This indicates that the location of the isosurface of vorticity magnitude $\hat{\omega}_{th}$ hardly changes with $\hat{\omega}_{th}$. Therefore, the threshold value should be chosen in this range.

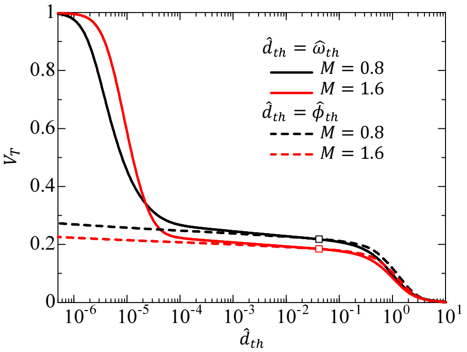

Figure 4. Normalized volume fractions of turbulent region V_T plotted against threshold $\hat{\omega}_{th}$ or $\hat{\phi}_{th}$ used for detecting turbulent fluids, $\hat{d}_{th}$ is $\hat{\omega}_{th}$ or $\hat{\phi}_{th}$.

Weak dependence of V_T on $\hat{\omega}_{th}$ is due to numerical error or pressure wave radiated toward outside from the TBL, which can also generate weak vorticity in non-turbulent fluids. The threshold should be determined so that these weak vorticity regions are not detected as turbulent fluids. Therefore, the threshold should be chosen from large values in the range $10^{-4} < \hat{\omega}_{th} < 10^{-1}$. In this study, the threshold value $\hat{\omega}_{th} = 0.04034$ is used to detect the irrotational boundary. $\hat{\omega}_{th} = 0.04034$ is shown with the squares in Fig. 4. We have already confirmed that the small change in $\hat{\omega}_{th}$ from this value hardly affects the location of the isosurface [20].

It has been shown that the passive scalar is also a good marker of turbulent fluids [36, 35], and isosurface of ϕ with the threshold ϕ_{th} determined by the dependence of V_T and ϕ_{th} can be also used as the irrotational boundary [36, 35]. V_T for turbulent fluids defined as $\phi > \phi_{th}$ is plotted against normalized threshold $\hat{\phi}_{th} = \phi_{th}/\overline{\phi}_c$ in Fig. 4. Unlike V_T computed with vorticity magnitude, V_T does not show rapid increase even for small $\hat{\phi}_{th}$. This is because the vorticity is computed with velocity gradient, which enhances small numerical error in velocity fields. Similar plots of V_T for vorticity magnitude and passive scalar were also obtained in incompressible TBLs and planar jets [45, 35]. The same value of normalized threshold is used for both vorticity magnitude and passive scalar. Thus, $\hat{\phi}_{th} = 0.04034$ is used in the analysis presented below. For these thresholds, both vorticity magnitude and passive scalar criteria result in almost same turbulent volume as shown in Fig. 4.

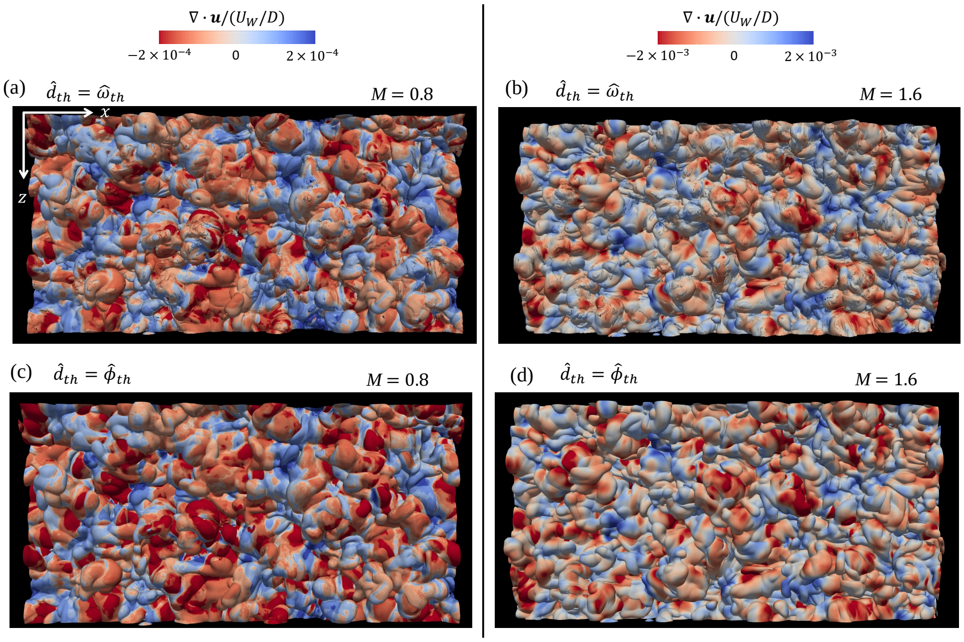

Figure 5. Visualization of irrotational boundary forming at the outer edge of the TNTI layer. Color represents dilatation $\nabla\cdot\boldsymbol{u}$. $\hat{d}_{th}$ indicates the threshold value of different detectors. The irrotational boundary detected by vorticity magnitude is shown in the upside for $M=0.8$ (a) and $M=1.6$ (b), detected by a passive scalar is shown in the bottom for $M=0.8$ (c) and $M=1.6$ (d).

The irrotational boundary detected by vorticity magnitude or passive scalar is visualized in the top view in Fig. 5. The color shows the dilatation $\nabla\cdot\boldsymbol{u}=-(D\rho/Dt)/\rho$, and the positive and negative values indicate fluid expansion and compression in the regions, respectively. The upper two pictures (Figs. 5 (a) and (b)) are irrotational boundary detected by vorticity magnitude, and the lower two (Figs. 5 (c) and (d)) are detected by a passive scalar. We can see that both expansion and compression regions coexist on the irrotational boundary, where the dilatation at $M=1.6$ is one order of magnitude larger than at $M=0.8$. The structures with various length scales can be found on the irrotational boundary, which implies the different length scales of turbulent motions underneath the TNTI layer [46, 47]. In the figures, the irrotational boundary detected by vorticity magnitude and passive scalar are very similar. This implies that the passive scalar can be used to detect the irrotational boundary in experiments when vorticity magnitude is difficult to measure.

Table 2. The mean thicknesses of the TNTI layer, VSL, and TSL normalized by the Kolmogorov scale near the TNTI layer [20].

M	TNTI layer δ_I	δ_{VSL}	δ_{TSL}
0.8	$15.4\eta_I$	$4.2\eta_I$	$11.2\eta_I$
1.6	$16.3\eta_I$	$4.2\eta_I$	$12.1\eta_I$

The statistics are computed as a function of the distance from the irrotational boundary. We use a local coordinate ζ_I whose origin $\zeta_I = 0$ is located on the irrotational boundary. The direction of ζ_I is normal to the irrotational boundary, which can be calculated by the gradient of enstrophy (squared vorticity magnitude) at the irrotational boundary as $\boldsymbol{n} = -\nabla\omega^2/|\nabla\omega^2|$, and positive and negative values of ζ_I point in the non-turbulent and turbulent region, respectively. ζ_I can be defined for each irrotational boundary point, and the statistics conditioned on values of ζ_I can be computed with ensemble average of all irrotational boundary points. Hereafter, subscript I denotes the conditional statistics, while the conditional average is denoted as $\langle\ \rangle_I$. Further details of the procedure for computing conditional statistics were presented in [35].

Since the statistical properties and geometry of the TNTI layer are characterized by the turbulence underneath the TNTI layer [46], the characteristics of turbulence at the location of $\zeta_I/\delta = -0.3$, which is under the TNTI, is used as reference quantities for the TNTI layer. Kolmogorov length scale at this location can be computed as $\eta_I = \langle\nu\rangle_I^{3/4}/\langle\varepsilon\rangle_I^{1/4}$ and the corresponding velocity scale is $v_{\eta_I} = \langle\nu\rangle_I\langle\varepsilon\rangle_I^{1/4}$. We choose $\zeta_I/\delta = -0.3$ because η_I and v_{η_I} weakly depend on ζ_I at this location while the conditional statistics within the the TNTI layer rapidly change with ζ_I [20].

Before we start to present the statistics for the passive scalar, we briefly describe the structure of the TNTI layer in the compressible TBLs studied here. This TNTI layer can be defined as a region where the vorticity magnitude is adjusted between the turbulent and non-turbulent regions. Furthermore, the TNTI layer can be divided into the VSL and TSL as shown in previous studies [15], and these inner structures of the TNTI layer can be distinguished with vorticity dynamics [48, 49]. Based on the derivative of the conditional mean vorticity magnitude $\langle\omega\rangle_I$, $-d\langle\omega\rangle_I/d\zeta_I$, the mean thickness of TNTI layer, δ_I, is quantified based on the location of 15% of the maximum value of $-d\langle\omega\rangle_I/d\zeta_I$. Then, the mean thicknesses of the VSL and TSL can be estimated by finding the averaged location of the boundary between the VSL and the TSL. This boundary is defined as the location of ζ_I at which the conditional mean value of the production term in the enstrophy transport equation is equal to the conditional mean value of the enstrophy diffusion term. We estimate the mean thickness of VSL, δ_I, as the distance from the irrotational boundary to the boundary between the TSL and VSL. Then, the inner region of the TNTI layer is detected as the TSL. The details of the quantification of the layer thickness are described in our previous paper [20]. The thicknesses normalized by η_I given in [20] are presented again in Tab. 2 because they are important for understanding the passive scalar statistics given below. The TNTI layer, VSL, and TSL have mean thickness of 15-16η_I, 4.2η_I, and 11-12η_I, respectively, for both Mach numbers. These values are close to those in incompressible free shear flows and shear free turbulence [43, 15, 50, 50].

3.3. Passive scalar mixing near turbulent/non-turbulent interface

Although the mean thicknesses of TNTI layer, VSL, and TSL slightly change with the Mach number, the differences are very small. Hereafter, we assume that the mean thicknesses of the TNTI layer, VSL, and TSL to be 15η_I, 4η_I, and 11η_I, respectively, for simplification of the discussions.

The conditional mean profiles of the passive scalar are shown in Fig. 6(a). $\langle\phi\rangle_I$ is almost zero in non-turbulent region, exhibits a sharp jump within the TNTI layer, and tends to be constant in the turbulent core region. This profile also confirms that the passive scalar can be used as a detector function of turbulent fluids. The conditional average of scalar dissipation rate $\langle\varepsilon_\phi\rangle_I$ are shown in Fig. 6(b), where the scalar dissipation rate ε_ϕ is defined as:

$$\varepsilon_\phi = 2D_m \frac{\partial\phi}{\partial x_j}\frac{\partial\phi}{\partial x_j}. \tag{13}$$

We can see that there is a peak of scalar dissipation rate near the boundary between TSL and VSL. As discussed in previous studies [43], the boundary between TSL and

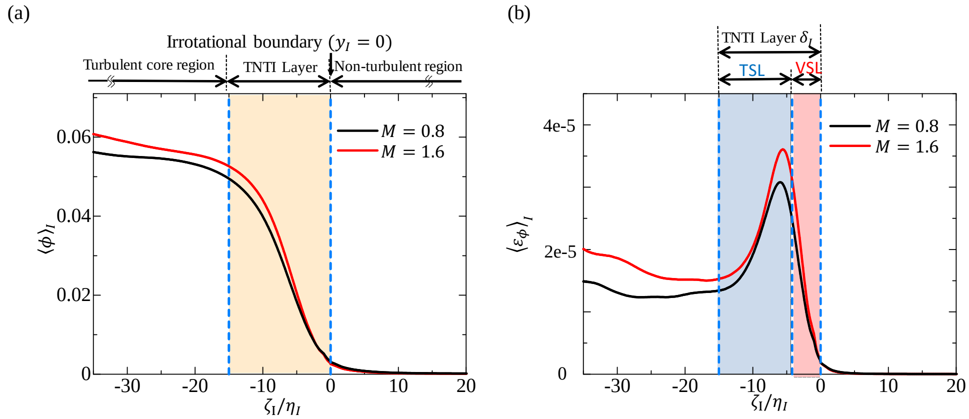

Figure 6. Conditional average of (a) passive scalar and (b) scalar dissipation rate.

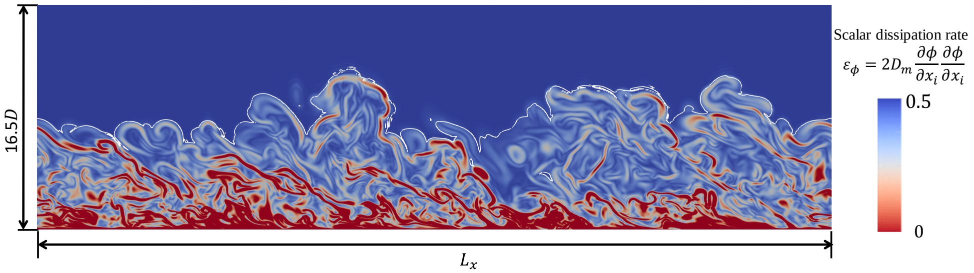

Figure 7. Instantaneous profile of scalar dissipation rate (color contour) and irrotational boundary (white line) on the $x-y$ plane at $M = 0.8$ and $Re_\theta = 2206$.

VSL is where a fluid with low-vorticity (low-scalar) from the non-turbulent region encounters a fluid with relatively high-vorticity (high-scalar) coming from turbulent core region. This causes the scalar gradient to be very large here. This can be also found in the instantaneous profile of scalar dissipation rate on $x-y$ plane for $M = 0.8$ (Fig. 7). There exist thin layers with high scalar dissipation rate near the irrotational boundary visualized by white lines, and these thin layers with high scalar dissipation rate near the TNTI layer are often aligned with the irrotational boundary.

Production terms of scalar gradient $G_iG_i = (\partial\phi/\partial x_i)^2$ and enstrophy can be written as $-G_iS_{ij}G_j$ and $\omega_iS_{ij}\omega_j$, respectively. These terms arise from the coupling between a strain tensor and vorticity or scalar gradient. The production rates are related to the effective contribution of the strain, and are defined as

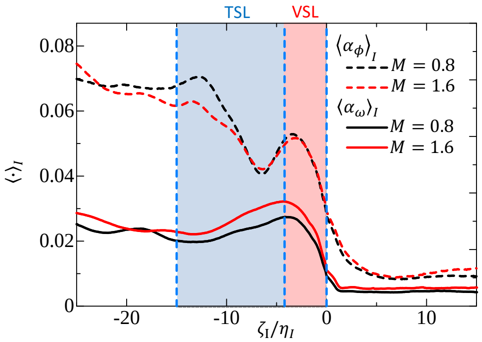

Figure 8. Conditional profiles of the production rate of enstrophy and scalar gradient.

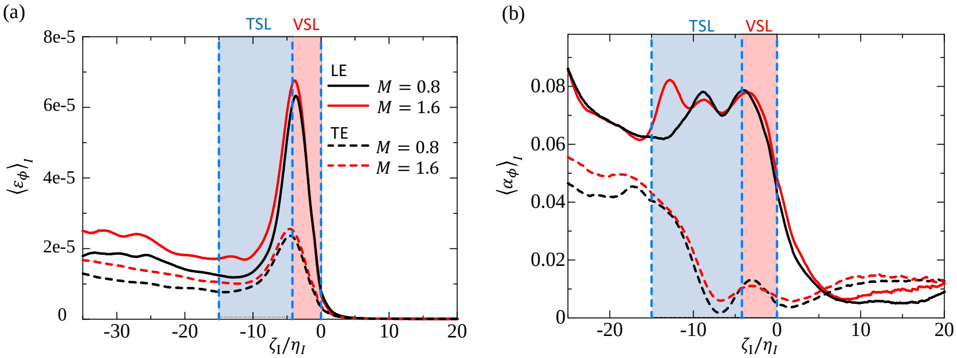

Figure 9. Conditional average of (a) scalar dissipation rate and (b) production rate of scalar gradient near the leading and trailing edges (LE: leading edge, TE: trailing edge).

$\alpha_\phi = -G_i S_{ij} G_j / G^2$ and $\alpha_\omega = \omega_i S_{ij} \omega_j / \omega^2$, which are also related to the alignment between strain eigenvectors and vorticity vector or scalar gradient [51]. Positive α_ϕ indicates dominant contribution of the compressive strain acting on the scalar gradient while positive α_ω indicates that vortex is stretched by the extensive strain. The conditional mean profiles of α_ϕ and α_ω are shown in Fig. 8. $\langle\alpha_\phi\rangle_I$ and $\langle\alpha_\omega\rangle_I$ are very similar for $M = 0.8$ and 1.6, and have positive values in the turbulent region. Thus, the enstrophy and scalar dissipation rate are produced via coupling between strain and vorticity vector or scalar gradient. Within the TNTI layer, $\langle\alpha_\phi\rangle_I$ and $\langle\alpha_\omega\rangle_I$ are larger than their non-turbulent values. $\langle\alpha_\phi\rangle_I$ and $\langle\alpha_\omega\rangle_I$ have a peak near the boundary between TSL and VSL.

From Fig. 7, there is a tendency that high scalar dissipation rate near the irrotational boundary appears more frequently when the irrotational boundary faces in the streamwise direction (x). The orientation of the irrotational boundary can be distinguished by the unit normal vector $\boldsymbol{n} = (n_x, n_y, n_z)$ [52]. For investigating the dependence on the interface orientation, the conditional statistics are computed separately for the leading edge and trailing edge, where leading edge defined as $n_x > 0.5$ faces the downstream direction and trailing edge $n_x < -0.5$ faces the upstream direction. The conditional averages of the scalar dissipation rate ε_ϕ and the production rate α_ϕ of G^2 for the leading edge and trailing edge are shown in Fig. 9. The scalar dissipation rate near the leading edge is higher than the one near the training edge, especially within the TNTI, in consistent with the visualization in Fig. 7. The production rate $\langle \alpha_\phi \rangle_I$ is also much higher near the leading edge, and $\langle \alpha_\phi \rangle_I$ near the training edge is very close to the non-turbulent value within the entire VLS and some part of TSL. The scalar gradient within the TNTI layer has a tendency of parallel alignment with the normal direction of the irrotational boundary [36] since the scalar rapidly changes across the TNTI layer. The orientation of the interface in relation to the mean flow direction has a strong influence on the strain field near the TNTI layer [52, 53]. In the TBLs developing over the moving wall, the turbulent fluid has a larger streamwise velocity u than the non-turbulent fluid. The leading edge is the TNTI that faces the downstream direction, where the turbulent fluid with larger streamwise velocity is often located in the upstream side of the leading edge with smaller streamwise velocity. Then, the turbulent fluid near the leading edge tends to have $\partial u/\partial x < 0$, which is related to the compressive strain in the streamwise direction. Because the scalar gradient tends to align with the normal direction of the irrotational boundary, the compressive strain near the leading edge tends to align with the scalar gradient, and the scalar gradient is effectively intensified by the compressive strain. In contrast, a fluid with $\partial u/\partial x > 0$ often appears near the trailing edge because the turbulent fluid in the downstream side of the trailing edge has a larger streamwise velocity, and this extensive strain makes the production rate of G^2 smaller near the

(a) $M = 0.8$

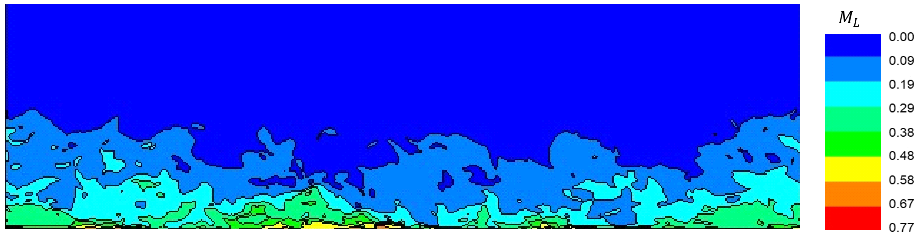

(b) $M = 1.6$

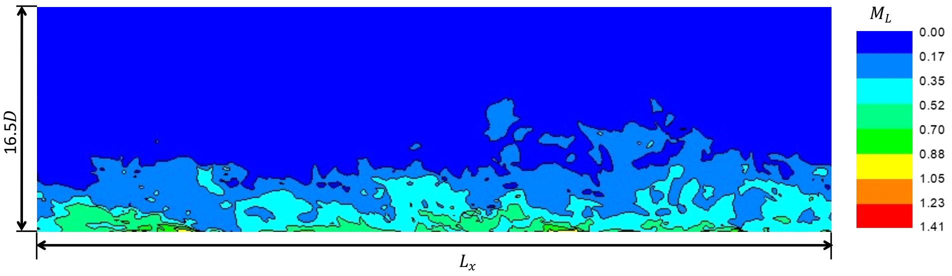

Figure 10. Isocontours of local Mach number M_L on the $x - y$ plane at $z = 0$ for free stream Mach number $M = 0.8$ (a) and $M = 1.6$ (b).

trailing edge. These dependences of $\langle \alpha_\phi \rangle_I$ also explain $\langle \varepsilon_\phi \rangle_I$, where the region with a small production rate $\langle \alpha_\phi \rangle_I$ has lower $\langle \varepsilon_\phi \rangle_I$. These dependences of $\langle \varepsilon_\phi \rangle_I$ and $\langle \alpha_\phi \rangle_I$ are similar to the relationship between the enstrophy production and TNTI orientation reported in the DNS of incompressible planar jets [52].

The passive scalar mixing process near the TNTI layer is shown to be very similar for $M = 0.8$ and $M = 1.6$. The isocontours of local Mach number defined based on the local velocity and sound speed as $M_L = |\mathbf{u}|/\sqrt{\gamma RT}$ are shown in Fig. 10. We can see that the local Mach numbers M_L are smaller than the Mach number based on the wall velocity in most regions of the TBL. The local Mach number are much smaller than 1 for $M = 0.8$ but exceeds 1 in the region very close to the wall for $M = 1.6$. Such large values of M_L cannot be seen in the intermittent region, where the TNTI appears. Small M_L in the intermittent region also explains weak effects of the compressibility near the TNTI. It was also shown that the properties of TNTI are hardly affected by compressibility even at the freestream Mach number of 2.8 [54]. Shocklets are expected to appear in the intermittent region when the freestream Mach number is much higher than our DNS [55]. DNS of supersonic planar jets showed that compressibility affects the TNTI via the change in density and temperature [32]. These compressibility effects through the fluid properties also agree with Morkovin's hypothesis [41].

4. Conclusion

The DNSs of temporally evolving compressible turbulent boundary layers are performed up to $Re_\theta \approx 2200$ at two Mach numbers, $M = 0.8$ and 1.6. The DNS results are used for studying the passive scalar near the TNTI.

The outer edge of TNTI, namely irrotational boundary, is well detected as an isosurface of vorticity magnitude or passive scalar, both of which are good markers of turbulent fluids. Isosurface of these quantities for detecting the irrotational boundary shows an excellent agreement with each other in visualization. The statistics are computed as a function of the distance from the irrotational boundary defined as an isosurface of vorticity magnitude, and discussed in relation to the inner structures of the TNTI layer, where the mean thicknesses of TNTI layer, VSL, and TSL, are about $15\eta_I$, $4\eta_I$, and $11\eta_I$, respectively, where η_I is the Kolmogorov length scale in the turbulent core region near the TNTI layer.

Conditional mean passive scalar also exhibits a sharp jump within the TNTI layer, and the highest conditional mean scalar dissipation rate appears near the boundary between the VSL and TSL. This indicates that the fluid locally entrained from non-turbulent region encounters the fluid coming from the turbulent region, where the difference in the passive scalar between these fluids creates large scalar gradients. It is also shown that the production rate of scalar gradient and enstrophy within the TNTI layer is as high as in the turbulent core region, and peaks in conditional averages of these quantities appear within the TNTI layer. Both visualization and conditional statistics show the dependence on the TNTI orientation for the scalar dissipation rate and the production rate of scalar gradient, both of which have a large value near the leading edge facing the downstream direction than the trailing edge facing the upstream direction. The production rate of scalar gradient within the TNTI layer of the trailing edge is comparable to the non-turbulent value, which causes lower scalar dissipation rate near the trailing edge. These tendencies are explained from the difference in streamwise velocity between turbulent and non-turbulent fluids in a similar way to the TNTI orientation dependence of enstrophy production (rate) given for incompressible planar jets [52, 53].

The conditional statistics confirmed that the direct influences of compressibility are small near the TNTI layer, and the profiles of the conditional statistics are qualitatively similar between incompressible and compressible turbulent boundary layers. These results indicate that models developed and tested in terms of local properties of the TNTI in incompressible flows, i.e., an entrainment model [56] and a mixing model [57], can be also successfully applied in compressible flows.

Acknowledgments

This work was partially supported by “Collaborative Research Project on Computer Science with High-Performance Computing in Nagoya University” and by MEXT KAKENHI Grant Number 18K13682 and 18H01367.

References

[1] Han J C, Dutta S and Ekkad S 2012 *Gas turbine heat transfer and cooling technology* (CRC Press)

[2] Wallace J M and Hobbs P V 2006 *Atmospheric science: an introductory survey* vol 92 (Elsevier)

[3] Smits A J and Dussauge J P 2006 *Turbulent shear layers in supersonic flow* (Springer Science and Business Media)

[4] Kirchhartz R M, Mee D J, Stalker R J, Jacobs P A and Smart M K 2010 *JJ. Propul. Power* **26** 57–66

[5] Barth J E, Wheatley V and Smart M K 2013 *AIAA J.* **51** 2147–2157

[6] Fox R O 2003 *Computational Models for Turbulent Reacting Flows* (Cambridge Univ. Pr.)

[7] Su L K and Clemens N T 1999 *Exp. Fluids* **27** 507–521

[8] Curl R L 1963 *AIChE J.* **9** 175–181

[9] Klimenko A Y and Bilger R W 1999 *Prog. Energy Combust. Sci.* **25** 595–687

[10] Cleary M J and Klimenko A Y 2009 *Flow, Turbul. Combust.* **82** 477–491

[11] Meyer D W 2010 *Physics of fluids* **22** 035103

[12] Tai Y, Watanabe T and Nagata K 2018 *Phys. Fluids* **30** 035108

[13] Corrsin S and Kistler A L 1955 *NACA Technical Report No. TN-1244*

[14] Bisset D K, Hunt J C R and Rogers M M 2002 *J. Fluid Mech.* **451** 383–410

[15] da Silva C B, Hunt J C R, Eames I and Westerweel J 2014 *Annu. Rev. Fluid Mech.* **46** 567–590

[16] Watanabe T, Riley J J and Nagata K 2016 *Phys. Rev. Fluids* **1** 044301

[17] Watanabe T, Naito T, Sakai Y, Nagata K and Ito Y 2015 *Phys. Fluids* **27** 035114

[18] Watanabe T, Sakai Y, Nagata K, Ito Y and Hayase T 2014 *Phys. Fluids* **26** 105111

[19] Gampert M, Kleinheinz K, Peters N and Pitsch H 2014 *Flow, Turbul. Combust.* **92** 429–449

[20] Zhang X, Watanabe T and Nagata K 2018 *Phys. Rev. Fluids* **3** 094605

[21] Guarini S E, Moser R D, Shariff K and Wray A 2000 *J. Fluid Mech.* **414** 1–33

[22] Martín M P 2007 *J. Fluid Mech.* **570** 347

[23] Kozul M, Chung D and Monty J P 2016 *J. Fluid Mech.* **796** 437–472

[24] Lee J H, Kwon Y S, Monty J P and Hutchins N 2014 Time-resolved PIV measurement of a developing zero pressure gradient turbulent boundary layer

[25] Kempf A, Klein M and Janicka J 2005 *Flow, Turbul. Combust.* **74** 67–84

[26] Wang Z, Lv Y, He P, Zhou J and Cen K 2010 *Comput. Fluids* **39** 1381–1389

[27] Carpenter M H and Kennedy C A 1994 *NACA Tech. Rep.*

[28] Kennedy C A and Carpenter M H 1994 *Appl. Numer. Math.* **14** 397–433

[29] Lodato G, Domingo P and Vervisch L 2008 *J. Comput. Phys.* **227** 5105–5143

[30] Bogey C and Bailly C 2009 *J. Fluid Mech.* **627** 129–160

[31] Wang Z, He P, Lv Y, Zhou J, Fan J and Cen K 2010 *Flow Turbul. Combust.* **84** 669–686

[32] Nagata R, Watanabe T and Nagata K 2018 *Phys. Fluids* **30** 105109

[33] Pope S B 2000 *Turbulent Flows* (Cambridge Univ. Pr.)

[34] Moser R D, Kim J and Mansour N N 1999 *Phys. Fluids.* **11** 943–945

[35] Watanabe T, Zhang X and Nagata K 2018 *Phys. Fluids* **30** 035102

[36] Gampert M, Boschung J, Hennig F, Gauding M and Peters N 2014 *J. Fluid Mech.* **750** 578–596

[37] Simens M P, Jiménez J, Hoyas S and Mizuno Y 2009 *J. Comput. Physics* **228** 4218–4231

[38] Wu X and Moin P 2010 *Phys. Fluids* **22** 085105

[39] Erm L P and Peter N J 1991 *J. Fluid Mech.* **230** 1–44

[40] Van Driest E R 1951 *J. Aeronaut. Sci.* **18** 145–160

[41] Morkovin M V 1962 *Méchanique de la Turbulence* **367** 380

[42] Pirozzoli S and Bernardini M 2011 *J. Fluid Mech.* **688** 120–168

[43] Watanabe T, Sakai Y, Nagata K, Ito Y and Hayase T 2015 *Phys. Fluids* **27** 085109

[44] Jahanbakhshi R, Vaghefi N S and Madnia C K 2015 *Phys. Fluids* **27** 105105

[45] Watanabe T, Sakai Y, Nagata K and Ito Y 2016 *Fluid Dyn. Res.* **48** 021407

[46] da Silva C B and Taveira R R 2010 *Phys. Fluids* **22** 121702

[47] Lee J, Sung H J and Zaki T A 2017 *J. Fluid Mech.* **819** 165–187

[48] Taveira R R and da Silva C B 2014 *Phys. Fluids* **26** 021702

[49] van Reeuwijk M and Holzner M 2014 *J. Fluid Mech.* **739** 254–275

[50] Silva T S, Zecchetto M and da Silva C B 2018 *J. Fluid Mech.* **843** 156–179

[51] Tsinober A 2009 *An informal conceptual introduction to turbulence* (Springer)

[52] Watanabe T, Sakai Y, Nagata K, Ito Y and Hayase T 2014 *J. Fluid Mech.* **758** 754–785

[53] Watanabe T, da Silva C B, Nagata K and Sakai Y 2017 *Phys. Fluids* **29** 085105

[54] Zhuang Y, Tan H, Huang H, Liu Y and Zhang Y 2018 *J. Fluid Mech.* **843**

[55] Duan L, Beekman I and Martín M P 2011 *Journal of Fluid Mechanics* **672** 245–267

[56] Watanabe T, Jaulino R, Taveira R R, da Silva C B, Nagata K and Sakai Y 2017 *Phys. Rev. Fluids* **2** 094607

[57] Watanabe T and Nagata K 2016 *Phys. Fluids* **28** 085103